Magnetic Resonance in Medicine 50:966–975 (2003)

Breast Tissue Differentiation Using Arterial Spin Tagging

David C. Zhu and Michael H. Buonocore*

An arterial spin tagging (AST) pulse sequence has been developed to measure T_1 and relative blood perfusion. This full sequence is composed of three sequences: selective tagging, nonselective tagging, and nontagging. Perfusion quantification error resulting from imperfect inversion and acquisition slice profiles has been addressed in the literature. In this work, the error is reduced through the application of optimized Shinnar-Le Roux (SLR) RF pulses and a semi-log linear regression data-processing technique. A threshold approach based on the breast tissue T_1 and relative blood perfusion is introduced to show that these two parameters can be applied to breast tissue differentiation and potentially to cancer detection. Magn Reson Med 50:966–975, 2003. © 2003 Wiley-Liss, Inc.

Key words: spin tagging; spin labeling; blood flow; perfusion; breast; T_1

An arterial spin tagging (AST) pulse sequence has been developed to measure T_1 and relative blood perfusion. These two parameters are used as the primary factors in the proposed technique for breast tissue differentiation. Perfusion quantification errors resulting from imperfect inversion and acquisition slice profiles are reduced through the application of optimized Shinnar-Le Roux (SLR) RF pulses and a semi-log linear regression data-processing technique (1–6).

Malignant tumors induce high-level angiogenesis, resulting in increased vascularity (7). The rapid growth of malignant tumors suggests that they have high metabolic rates and thus require an increased supply of nutrients and oxygen, as well as increased effort to remove waste materials. Therefore, higher blood perfusion and blood volume percentage in malignant tumors are expected (8–10). High water content leads to a long MR spin-lattice relaxation time (T_1). Therefore, T_1 and relative blood perfusion are two important factors that can be used in determining breast cancer malignancy. The proposed method for distinguishing between normal and abnormal tissues is based on the expectation that malignant tumors have a higher water content than normal tissues, and higher perfusion than both normal tissues and benign lesions.

BACKGROUND

The primary goal of the present AST technique is to measure perfusion, which is defined as the milliliters of arterial blood delivered per second per milliliter of tissue (11). Capillaries penetrate each voxel in various directions. Therefore, perfusion represents the combined activity of the flow of the capillaries and other small vessels within a voxel. The Kety-Schmidt model is used to approximate the activity of the water molecules. In this model, water molecules in blood vessels entering a region of breast tissue mix thoroughly with water molecules outside the vessels before they leave the region (12–14). The Bloch equation for the water magnetization in a slice of tissue after any RF perturbation was deduced by Detre et al. (15):

$$\frac{dM(t)}{dt} = \frac{M_0 - M(t)}{T_1} + fM_a(t) - f\frac{M(t)}{\lambda} \qquad [1]$$

where $M(t)$ = the longitudinal water magnetization of a voxel of tissue at time t, M_0 = the value of $M(t)$ under fully relaxed conditions, T_1 = the spin-lattice relaxation time constant of the tissue, M_a = the longitudinal water magnetization of arterial blood from outside of the slice measured, f = perfusion in milliliters of arterial blood per second per milliliters of tissue (with dimensions of s^{-1}), λ = the ratio of water concentration between breast tissue overall and the arterial blood within it, specifically (moles of water per milliliters of tissue)/(moles of water per milliliters of arterial blood).

The above equation does not include the magnetization transfer terms presented in a later publication by Detre et al. (16).

Theory of Pulse Sequence Design

Various spin tagging techniques have been used to estimate perfusion f (or f/λ) (15–21). These techniques are all based on three different spin states: equilibrium, saturation, and inversion. They can also be categorized as on- and off-slice tagging sequences.

The AST method presented here is based on two of these three states: equilibrium and inversion, which should give the maximum spin signal contrast. On-slice rather than off-slice spin tagging was chosen so that the measurement would be sensitive to the perfusion effect from both sides of the acquisition slice. Parameters T_1 and f/λ in Eq. [1] are estimated from two spin tagging sequences (the selective and nonselective sequences) and the nontagging sequence. The slices are investigated one at a time (referred to as the slice of interest in the following discussion). For the selective sequence, spins in the slice of interest are inverted first. Then signal from the same slice is acquired after a delay time. This delay time is varied to obtain the magnetization recovery curve. The only difference between the selective and nonselective sequences is that spins in the latter are inverted within the entire sensitive volume of the RF transmit coil. For the nontagging sequence, there is no spin inversion before acquisition. Since the spins entering the slice of interest are not perturbed during the selective sequence, they are in equilibrium. Then,

Department of Radiology, UC–Davis Medical Center, Sacramento, California.

Grant sponsor: U.S. Army Medical Research and Materiel Command; Grant number: DAMD 17-97-1-7030.

*Correspondence to: Michael H. Buonocore, M.D., Ph.D., Dept. of Radiology, UC–Davis Imaging Center, Rm 1215, 4701 X Street, Sacramento, CA 95817. E-mail: mhbuonocore@ucdavis.edu

Received 19 September 2002; revised 5 May 2003; accepted 21 May 2003.
DOI 10.1002/mrm.10616
Published online in Wiley InterScience (www.interscience.wiley.com).

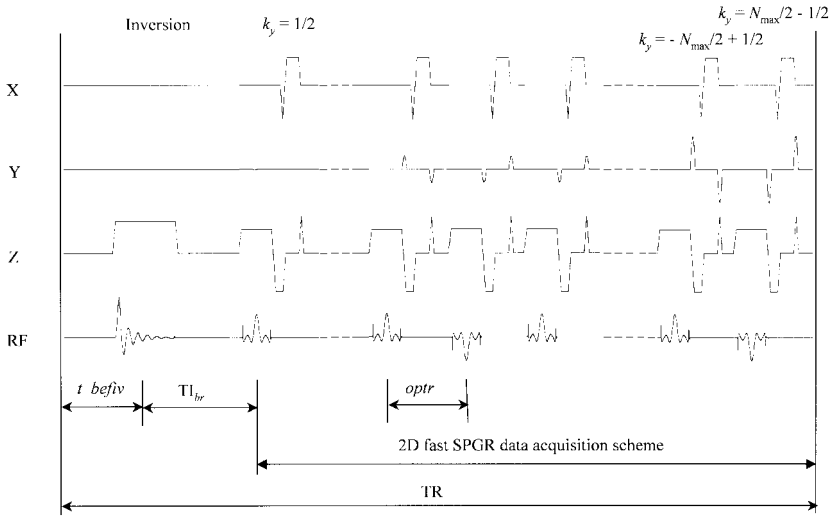

FIG. 1. The fast SPGR-based AST sequence. The parameter TR is fixed at 2.7 s by default. An inversion tagging RF pulse is applied first, followed by phase-encoding steps starting around zero *k*-space. The time TI_{br} is changed by changing *t_befiv*. To show the details, the RF acquisition pulses are magnified, and *t_befiv* and TI_{br} are longer than they appear. N_{max} is the total number of k_y lines.

$$M_a(t) = M_a^0$$

where, $M_a{}^0$ = the value of $M_a(t)$ under the fully relaxed condition. In the Kety-Schmidt model, it is assumed that spins in the arterial blood entering the slice are able to mix thoroughly with spins in the surrounding breast tissue before they leave the slice (12–14,22). Thus, in equilibrium:

$$fM_a^0 = f\frac{M_0}{\lambda}$$

Equation [1] then becomes

$$\frac{dM(t)}{dt} = M_0\left(\frac{1}{T_1} + \frac{f}{\lambda}\right) - M(t)\left(\frac{1}{T_1} + \frac{f}{\lambda}\right) \qquad [2]$$

Equation [2] has the form of the standard Bloch equation

$$\frac{dM(t)}{dt} = \frac{M_0 - M(t)}{T_{1s}}$$

with

$$\frac{1}{T_{1s}} = R_{1s} = \frac{1}{T_1} + \frac{f}{\lambda} \qquad [3]$$

where T_{1s} is the apparent spin-lattice relaxation time measured through the selective sequence. The subscript "*s*" denotes the T_1 and the R_1 values measured through the selective sequence. In Eq. [3] above, the effect of the mean transit time τ of spins in the tagged slice, as described by Bauer et al. (21) in the arterial system, is assumed to be negligible for the T_{1s} calculation.

During the nonselective sequence, spins are inverted within the entire sensitive volume of the RF coil. The spins inside and outside the slice of interest thus have the same magnetization. Then

$$fM_a(t) = f\frac{M(t)}{\lambda}$$

and Eq. [1] becomes

$$\frac{dM(t)}{dt} = \frac{M_0 - M(t)}{T_1}$$

The T_1 measured in this case is the true T_1 without the influence of blood flow, which is denoted as

$$T_{1n} = T_1 \qquad [4]$$

and

$$R_{1n} = \frac{1}{T_{1n}} \qquad [5]$$

The subscript "*n*" denotes the T_1 and R_1 values measured through the nonselective sequence, which distinguishes them from the selective sequence. Based on the R_{1s} and R_{1n} values obtained from the two tagging sequences, the relative perfusion is

$$\frac{f}{\lambda} = R_{1s} - R_{1n} \qquad [6]$$

The term f/λ is the fraction of water replaced per second in a voxel in the direction perpendicular to the slice. In the above equation and its derivation, it is assumed that the T_1 of blood is the same as that of tissue (23). Compared to normal breast tissue and benign lesions, a higher f/λ is expected in malignant tumors.

MATERIALS AND METHODS

AST Pulse Sequence Implementation

For the AST sequence, an inversion RF pulse is applied first to tag the spins, and then data are acquired for the entire image using a fast spoiled gradient-recalled (SPGR) symmetric-*k* space data acquisition scheme (Fig. 1). Data acquisition starts at the *k*-space line closest to $k_y = 0$, and then alternates below and above this k_y line until the lowest and highest k_y lines. This allows the signal of the

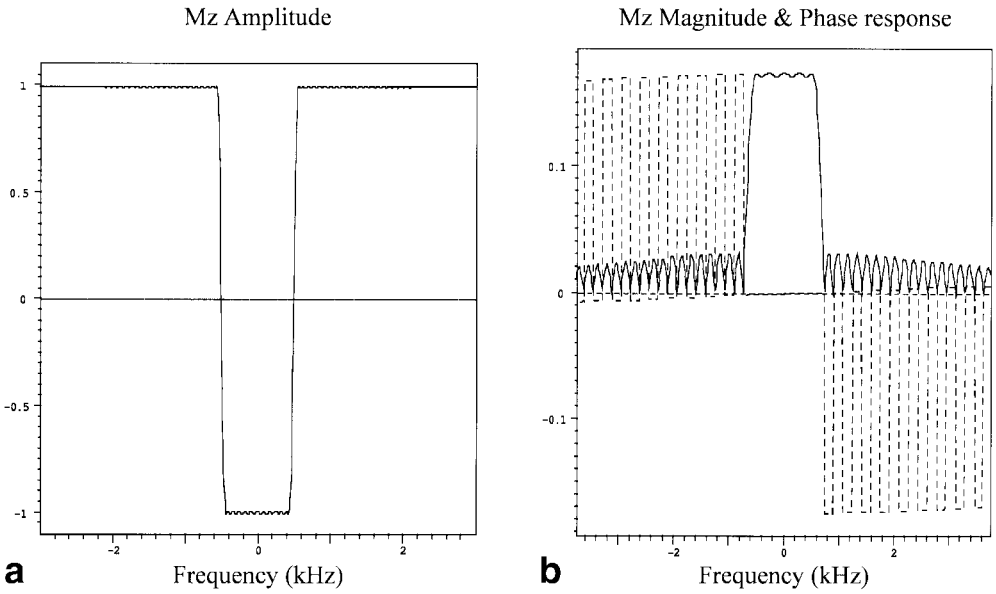

FIG. 2. SLR 180° inversion and 10° data acquisition RF pulses frequency response based on simulation: (**a**) The near rectangular frequency response based on the longitudinal magnetization for the inversion pulse, and (**b**) the magnitude of the frequency response based on the longitudinal magnetization and the associated phase for the data acquisition RF pulse.

reconstructed image to have the highest weighting on the data points at the beginning of the acquisition. Thus, the effective time of inversion has a wide range to map the T_1 recovery curve.

For the selective sequence, the slice of inverted magnetization is created by applying an SLR inversion pulse in the presence of the slice-selection gradient. For the nonselective sequence by applying this SLR inversion pulse without an associated slice-selection gradient, a nonselective slab containing inverted spins within the entire sensitive volume of the transmit RF coil is created. The data acquisition for the nontagging sequence is designed simply by setting the amplitude of the inversion RF pulse and the associated *z*-gradient pulse to zero, thus keeping the same timing as used in the other two sequences.

Optimized RF inversion and acquisition pulses were designed based on the SLR algorithm (24). The goal was to achieve sharp rectangular slice profiles so that the spins that are tagged are basically the spins that are measured with the selective sequence. This inversion pulse is a maximum-phase pulse with a 15.6-ms pulse width, 0.95-kHz bandwidth, 1.50% ripple in the pass band, 0.40% ripple in the stop band, and 180° flip angle. This acquisition pulse is a spin-echo linear-phase pulse with a 6.4-ms pulse width, 1.25-kHz bandwidth, 5% ripple in the pass band, 5% ripple in the stop band, and 10° flip angle (Fig. 2). To reduce the impact on the overall scan time, the acquisition pulse must be kept short, and thus its slice profile is less ideal than the inversion pulse. The slice profile issue that can contribute to perfusion quantification error is addressed in data processing.

In each scanning session, approximately 10 equally spaced coronal slice locations in the breasts are imaged with a total scan time of approximately 25 min. Both breasts are scanned simultaneously. At each slice location, 61 images are acquired sequentially with a repetition time (TR) of 2.7 s, using the AST sequence (Fig. 3). Twenty-eight images are acquired through the selective sequence, and then the same number of images through the nonselective sequence and then five images through the nontagging sequence. For either the selective or nonselective sequence, seven different choices of inversion time (TI_{br}'s) are used for the 28 images. Four images are acquired at each choice of TI_{br}.

Half-phase field of view (FOV) data acquisition is used to achieve the necessary high resolution without any sacrifice of the scan time. The FOV in the *y* direction is only half of that in the *x* direction. This takes advantage of the rectangular FOV in bilateral breast imaging.

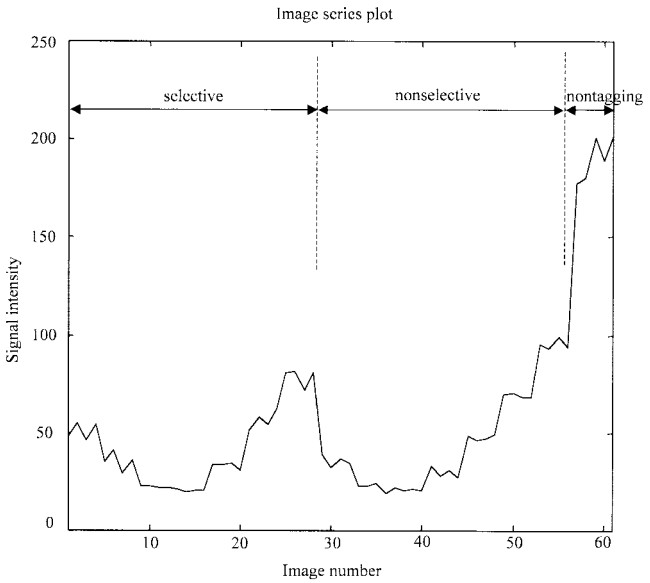

FIG. 3. Image series plot using the fast SPGR-based AST sequence. This plot shows the signal at the same pixel across the 61 images acquired using the full sequence. This full sequence is composed of selective, nonselective, and nontagging sequences. For either the selective or nonselective sequence, seven TI conditions are used. Four repeated images are acquired at each TI condition. Images are acquired in a continuous manner with TR = 2.7 s.

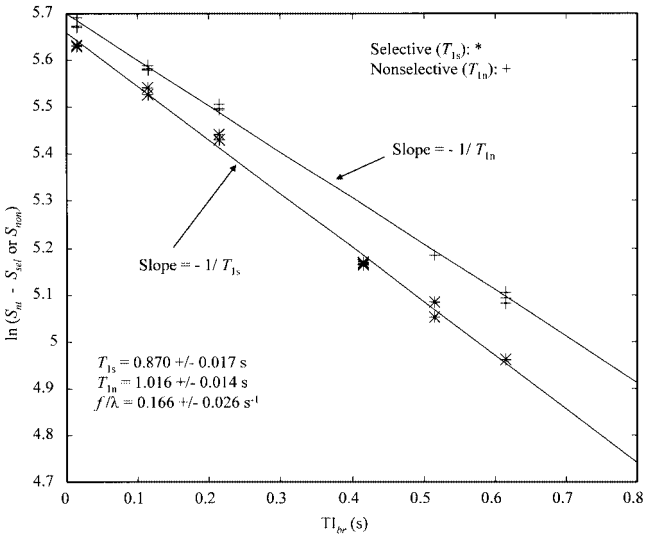

FIG. 4. An example of semi-log linear regression for T_1 calculation. This figure shows an example of the application of the semi-log linear regression method in calculating T_1 values (T_{1s} in the selective sequence, and T_{1n} in the nonselective sequence) and the relative perfusion rate f/λ. TI_{br} is the starting time of image acquisition after the spins are inverted. S_{nt} is the average signal intensity at one pixel from the last three images at the nontagging sequence. S_{sel} is the signal intensity at the same pixel from one of the steady-state images at the selective sequence. S_{non} is the signal intensity at the same pixel from one of the steady-state images at the nonselective sequence.

Numerical Technique for f/λ Estimation

The value of f/λ is the difference between the R_{1s} and R_{1n} values, as expressed in Eq. [6]. At each pixel, all dynamic images are used to calculate the R_{1s} or R_{1n} value based on a statistical semi-log linear regression technique. This technique not only provides the necessary statistical information for analysis, it also reduces perfusion quantification error resulting from the uncertainty of the effective TIs and the geometric mismatch between the inversion and acquisition slice profiles.

This technique was developed based on a comparison between the signal from noninverted spins in the nontagging sequence and the signal from inverted spins in the selective or nonselective sequence (Fig. 4). For either tagging sequence, the last three of the four acquired images at each choice of TI are nearly at steady state and are extracted for analysis. For the nontagging sequence, the last three of the five acquired images are nearly at steady state, and their mean is used for analysis. Using the mean of three images instead of a single image helps to improve the signal-to-noise ratio (SNR).

The semi-log linear regression equations, which are derived in the Appendix, are shown below based on two arbitrary data points (the ith and jth data points) of the T_1 recovery curve:

$$R_{1s} = \frac{1}{T_{1s}} = -\frac{\ln(S_{nt} - S_{sel}(i)) - \ln(S_{nt} - S_{sel}(j))}{TI_{br}(i) - TI_{br}(j)} \quad [7]$$

$$R_{1n} = \frac{1}{T_{1n}} = -\frac{\ln(S_{nt} - S_{non}(i)) - \ln(S_{nt} - S_{non}(j))}{TI_{br}(i) - TI_{br}(j)} \quad [8]$$

where S_{nt} = the average signal intensity at a pixel from the steady-state images from the nontagging sequence, $TI_{br}(i)$ or $TI_{br}(j)$ = the starting time for image data acquisition after spin inversion at the ith or jth timing condition, $S_{sel}(i)$ or $S_{sel}(j)$ = the signal intensity at a pixel for a steady-state image at the ith or jth timing condition of the selective sequence, and $S_{non}(i)$ or $S_{non}(j)$ = the signal intensity at a pixel for a steady-state image at the ith or jth timing condition of the nonselective sequence.

The TI_{br} defined in the sequence (Fig. 1) is used in the above equation instead of TI as in Eq. [A8]. During the selective or nonselective sequence, signal is acquired along the recovery curve for the multiple phase-encoding steps. Although the first encoding step (at TI_{br}) is the center of k-space, the effective TI is shifted from TI_{br}. The amount of shift depends on the T_1 of the pixel and the section of the recovery curve. The subtraction of $TI_{br}(i)$ and $TI_{br}(j)$ eliminates the TI shift contributed by the pixel T_1. Thus, the R_{1s} or R_{1n} calculation error due to the uncertainty of the effective TIs is reduced through the subtraction of $TI_{br}(i)$ and $TI_{br}(j)$.

Equation [7] also reduces the R_{1s} (or T_{1s}) quantification error resulting from the geometric mismatch between the inversion and data acquisition slice profiles. The T_{1n} quantification does not have this slice profile mismatch problem, because the RF inversion pulse inverts spins within the entire sensitive volume of the RF transmit coil. For the selective sequence, the geometric mismatch between the inversion and acquisition slice profiles can lead to signal contamination by signal from noninverted or partially inverted spins. Assuming the RF inversion pulse is so optimized that the fraction of partially inverted spins can be neglected, the measured signal can be modeled as

$$S_{sel_{meas}} = (1 - err) \cdot S_{sel} + err \cdot S_{nt} \quad [9]$$

where S_{sel} = the signal of a pixel if there is no slice profile mismatch, $S_{sel_{meas}}$ = the signal of the same pixel measured, and err = the fraction of error due to a slice profile mismatch.

The above model approximates the effect of a sharp rectangular inversion slice profile and a less ideal acquisition slice profile that were designed in this sequence.

Based on the above model, the following is derived in the Appendix (Eq. [A10]):

$$\ln(S_{nt} - S_{sel}(i)) - \ln(S_{nt} - S_{sel}(j)) = \ln(S_{nt} - S_{sel_{meas}}(i)) - \ln(S_{nt} - S_{sel_{meas}}(j)).$$

Therefore, either S_{sel} or $S_{sel_{meas}}$ can be used to calculate R_{1s} through Eq. [7]. In other words, by applying the semi-log linear regression method, the problem of a geometric mismatch between the inversion and acquisition slice profiles is eliminated. For simplicity of the notations, the subscript "*meas*" is not used in Eqs. [7] and [8]; rather, S_{sel} and S_{non} in these two equations actually represent the signals measured at a pixel.

Methods to Distinguish Between Normal and Abnormal Tissue

After the values of T_{1s}, T_{1n}, and f/λ at all pixels on each slice are calculated, the corresponding T_1 image, the per-

fusion image based on f/λ, and the error perfusion image based on the standard deviation (SD) of f/λ are constructed. These images are used for the recognition of probable cancer regions through a visualization computer program called BreastView, which was developed on an SGI workstation based on C language, X Window System, and Motif 1.2. This program is implemented with a threshold technique, as discussed below (4,5).

Since it is likely that a tumor will grow into several adjacent voxels, these voxels should have similar tissue characteristics. Specifically, they should have high T_1 values that are approximately equal to each other, and high perfusion rates. When a pixel is found to have a high T_1 and a high f/λ, and the SD of the f/λ is low (based on predefined thresholds), this pixel is considered to be a possible cancer pixel. Its surrounding pixels within the same slice and across slices would be checked to see whether they have similar characteristics. The level of suspicion (which is arbitrarily defined as the chance of being cancerous) for this pixel is calculated based on the percentage of its surrounding pixels (including this central pixel) containing similar suspicious characteristics. For a typical pixel, there are 27 pixels to check. For a pixel on an edge slice, there are 18 pixels to check. A 5% contribution from the background is always applied. For example, if a suspected cancer pixel has six adjacent pixels with similar characteristics out of the 27 surrounding pixels, its level of suspicion is 30.9%. By applying this method to all pixels in all slices, maps of suspicion are created. If a pixel has a level of suspicion exceeding a cutoff value (e.g., 20%), this pixel would be labeled as a probable cancer pixel.

Phantom and In Vivo Studies

The ability of the AST sequence to measure T_1 and perfusion was verified through studies with a flow phantom, normal subjects with normal breasts, and patients with abnormal breast masses. Most of these studies were performed on a Signa Advantage 1.5T GE MR system, and the rest were performed on a Signa Horizon LX 1.5T GE MR system (GE Medical Systems Inc., Milwaukee, WI). A dual phased-array breast imaging RF receiving coil (Medical Advance Inc., Milwaukee, WI) was used for the breast studies.

The following parameters were used in all of the studies: TE = 9.244 ms, TR = 16.62 ms for the phase-encoding steps, receiving bandwidth = $\pm$31.25 kHz, flip angle = 10°, slice thickness = 3 mm, FOV = 34 cm $\times$ 17 cm, and matrix resolution = 256 $\times$ 120. The TI starts with 615 ms and decrements to 15 ms, with a step size of 100 ms.

Perfusion studies using a controllable flow phantom were the first set of verification studies done. A flow phantom was assembled from a kidney dialysis cylinder. This dialysis cylinder is composed of artificial capillaries with membranes that allow the exchange of molecules during dialysis for kidney patients. Water molecules and small ions, such as the manganese and chlorine ions that were used in this experiment, can move freely through these membranes. The cylinder has a length of 25 cm, an internal diameter of approximately 5 cm, approximately 12000 capillaries (200-μ inner diameter and 40-μ membrane wall thickness for each capillary) (Fresenius Medical Care, Lexington, MA). The internal cross-section ratio between the cylinder and the capillaries was calculated to be approximately 5.21. The fluid used in the phantom was purified drinking water doped with manganese chloride to obtain a T_1 value of approximately 895 ms, which is within the range of T_1 value of tissue. To facilitate the physical measurement, the perfusion of the flow phantom was verified in only one direction, rather than the multiple directions that occur in actual tissue. The flow went through the capillaries from one end of the dialysis cylinder, fed through long rubber tubes, and was driven by an external electrical mechanical pump outside the magnet room. The flow rate was controlled by adjustments to the mechanical pump and was measured using a stop watch and a graduated cylinder.

Eighteen subjects participated in the breast imaging studies. All volunteers signed the consent forms approved by the Institutional Review Board at the University of California–Davis. For each study, some simple but effective procedures were used to reduce motion artifacts: the volunteer was strapped onto the scan table in a prone position, and was instructed to breathe smoothly during scanning and remain motionless. The AST scan was performed in a coronal view for each study. In addition to the AST scan, other examinations using traditional clinical techniques were also performed. A T_1-weighted, multislice, spin-echo axial scan was used as a localizer to provide an overview of the whole breasts and neighboring tissues, and to help detect the existence of any abnormal mass. A fast spin-echo coronal scan with proton density-weighted and T_2-weighted dual echoes was used to provide traditional clinical breast images. The slice locations of these images were the same as those used for the AST sequence. After the imaging study, a biopsy was performed on all patients with benign and malignant masses, with the exception of one benign case.

RESULTS

Phantom Studies

The flow phantom studies showed a clear linear relationship between f/λ measured with the AST technique and the actual flow applied within the range of tissue perfusion (Fig. 5).

Human Subject Studies

Eighteen subjects (11 patients and seven normal volunteers), participated in the breast studies. Three patients and two volunteers were eliminated from the analysis because the studies were not done according to protocol, there was excessive motion during scanning, the abnormal mass was too close to the chest wall to be measured reliably, or no patient biopsy was performed to confirm the results of the MR study. There were a total of 13 useful cases available for analysis, including three cases of normal breast, eight cases of benign lesions, and two cases of malignant masses. Three sample case studies (one with normal breasts, one with benign abnormal masses, and one with malignant tumors) are presented first, followed by a summary of the studies.

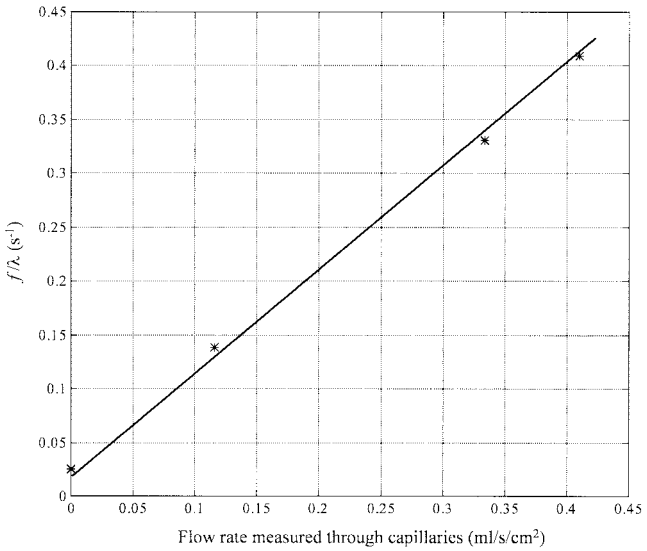

FIG. 5. Results from the kidney dialysis phantom perfusion study. The AST sequence was applied at four different low flow rates with 0, 0.0222, 0.0640, and 0.0787 ml/s/cm^2 through the cylinder, or equivalently 0, 0.116, 0.333, and 0.410 ml/s/cm^2 through all the capillaries based on the internal cross-section ratio of 5.21 between the cylinder and capillaries. The corresponding f/λ values calculated were 0.0251, 0.138, 0.331, and 0.409 s^{-1}.

Normal

In this study, all images acquired showed well-separated fat and nonfat regions. Regions of interest (ROIs) can be easily isolated for the characteristic comparison between fat and nonfat tissues of the breast. The ROIs (35 mm^2) were identified from all 10 slices acquired from the AST sequence. The f/λ and T_{1n} distributions for this study are summarized in Table 1. Voxels containing nonfat tissue in general have higher T_{1n} and f/λ values than voxels containing fatty tissue.

Benign Abnormal Mass

A rod-shaped abnormal mass was observed in the breast of a healthy volunteer. Based on 10 years of monitoring, this mass had been diagnosed to be benign before the perfusion study was performed. ROIs (35 mm^2) were isolated from the edge and the center of the abnormal mass, as well as the nonfat area outside the abnormal mass, for the tissue MR characteristic comparison. The f/λ and T_{1n} distributions for these different tissues are summarized in Table 2. For this case study, the lesion center in general had a higher perfusion rate (f/λ) than the lesion edge and the nonfat regions.

Table 1
The f/λ and T_{ln} Summary for a Study of Normal Breasts

	Mean of T_{ln} (s)	STD of T_{ln} (s)	Mean of f/λ (s^{-1})	SD of f/λ (s^{-1})
Fat	0.435	0.207	−0.005	0.135
Nonfat	1.446	0.403	0.033	0.044

Table 2
The f/λ and T_{ln} Summary for a Study of a Benign Abnormal Breast Mass

	Mean of T_{ln} (s)	STD of T_{ln} (s)	Mean of f/λ (s^{-1})	SD of f/λ (s^{-1})
Lesion center	0.813	0.053	0.057	0.018
Lesion edge	0.615	0.140	0.034	0.018
Nonfat tissue	1.142	0.487	0.013	0.025

Malignant Tumor

In this study, three slice locations centered around an abnormal mass were studied. The probable cancer regions were identified according to the image processing and visualization techniques discussed above, and were labeled by color mapping and overlay onto the clinical images (Fig. 6). These regions were close to the abnormal mass, which was palpated and was later confirmed by needle biopsy to be malignant. ROIs (35 mm^2) were isolated at the tumor, nonfat regions outside the tumor as well as fat regions for tissue MR characteristic comparison. Figure 7 shows the f/λ and T_{1n} distributions for these different areas, which are summarized in Table 3. As shown in Fig. 7, fat can easily be differentiated based on T_{1n} value alone, because its T_{1n}'s are much lower than those of the other two groups of tissue. The f/λ values for fat have a wide range, and thus f/λ does not provide any benefit for fat tissue recognition. Since tumor tissue is nonfat tissue, and should have T_{1n} values in the range of healthy nonfat tissue, the overlap between fat and tumor is minimal. However, to distinguish between tumor tissue and nonfat tissue, both the T_{1n} and f/λ values should be used. For example, as shown in Table 3 and Fig. 7, both the T_{1n} and f/λ values in tumor tissue are relatively higher than those in nonfat tissue, although there is some overlap.

Human Subject Studies Summary

For all human subject studies, the probable cancer pixels were identified based on the following criteria:

$T_{1n} > 0.5$ s
$f/\lambda > 0.1$ s^{-1}
STD of $f/\lambda < 0.1$ s^{-1}
Suspicion level threshold $> 20\%$.

The above T_{1n} threshold was chosen based on a comparison of T_{1n} distribution between fat and nonfat tissue in the normal cases. The above f/λ and STD of f/λ thresholds were chosen based on the f/λ distribution in the malignant cases. The suspicion level threshold was chosen based on the comparison between malignant and benign cases. These thresholds were based on observations rather than vigorous statistical analysis, which would require more case studies.

The results of 13 studies are summarized in Table 4. As shown in the table, there were two true positives, zero false negatives, three false positives, and eight true negatives. Therefore, this pilot study shows a 100% true-positive fraction and a 27.3% false-positive fraction.

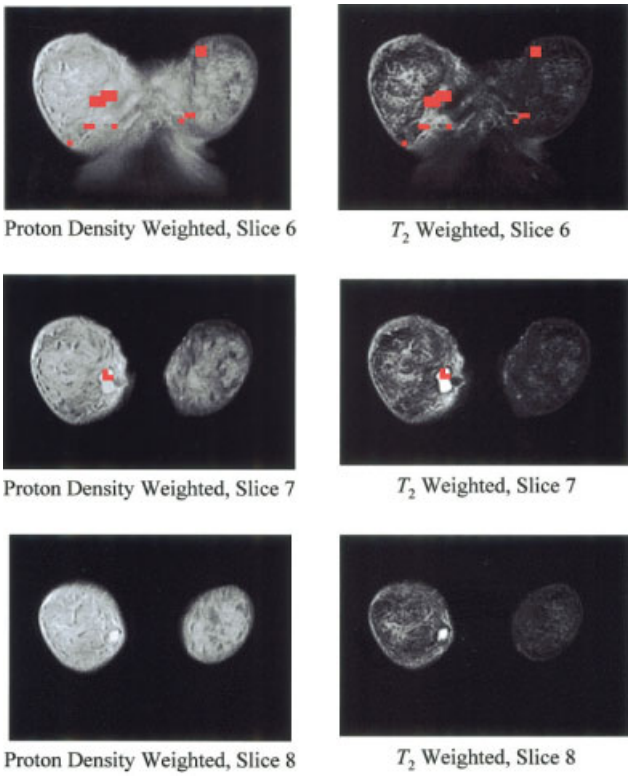

FIG. 6. Probable cancer region color mapping. The identified suspected cancer pixels are mapped onto the high-resolution traditional clinical MR images according to their corresponding slice locations. These images are from three consecutive 3-mm slices with an interslice distance of 10 mm.

DISCUSSION

The flow phantom studies show that the AST sequence can be applied to measure perfusion activity accurately. The human subject studies show that the AST sequence and the analytical technique can be applied to tissue classification and tumor identification. The results from the human subject studies confirm the expectation that malignant tumors have a higher water content than normal tissues, and higher perfusion than both normal tissues and benign lesions.

Table 3
The f/λ and T_{1n} Summary of a Malignant Breast Tumor Study

	Mean of T_{1n} (s)	STD of T_{1n} (s)	Mean of f/λ (s^{-1})	SD of f/λ (s^{-1})
Fat	0.385	0.085	−0.177	0.592
Nonfat	0.842	0.392	0.035	0.266
Tumor	1.145	0.372	0.111	0.142

The probable cancer pixel identification based on the thresholds of T_{1n}, f/λ, STD of f/λ, and the suspicion level provides a feasible approach for cancer recognition. This technique is most useful if the number of cases studied is limited. However, if a large pool of case studies is available, statistical techniques, such as the Bayesian decision technique, can be used for cancer identification (5,25). The Bayesian technique can be extended to the receiver operating characteristic (ROC) curve, which is commonly used for evaluating diagnostic algorithms in radiology.

For the selective sequence, the same slice thickness is applied for both inversion and acquisition to increase the sensitivity to perfusion. This avoids the transit delay that occurs between the tagging and acquisition regions if the inversion slice is thicker than the acquisition slice (26). However, this leads to the problem of slice-profile mismatches. This issue has been addressed by Frank et al. (27), Schepers et al. (28) (with an emphasis on RF pulse design), and Sidaros et al. (29) (with an emphasis on postprocessing). In the current work, both approaches were applied through the use of optimized RF pulses and a statistical semi-log linear regression postprocessing technique. Schepers et al. (28) showed that adiabatic pulses could produce better slice profiles than sinc and SLR

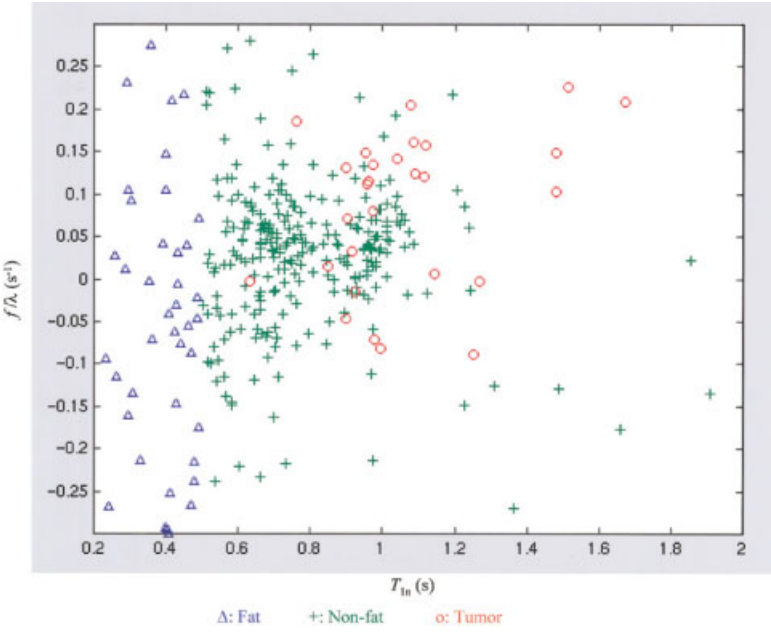

FIG. 7. The f/λ and T_{1n} distribution for breast tissue with a malignant tumor. The thresholds of 0.5 s T_{1n} and 0.1 s^{-1} f/λ are used to identify the probable cancer pixels.

Table 4
Summary of Breast Case Studies

Date of study	Subject referred by	Palpable ? (yes or no)	Seen on clinical MRI?	Level of suspicion based on T_{ln} and f/λ	Assessment based on suspicion level	Abnormal mass type
05/03/97	Physician	No	Yes	Low	Negative	Benign (fibroadenoma)
05/23/97	Physician	Yes	Indeterminable	Moderate High	Positive	Malignant (ductal carcinoma)
08/01/97	Physician	Yes	No	High	Positive	Malignant (ductal carcinoma)
11/15/97	Physician	Yes	No	Low	Negative	Benign
12/10/97	Physician	Yes	No	High	Positive	Benign
04/13/98	Physician	Yes	Indeterminable	Moderate High	Positive	Benign
07/27/98	Physician	Yes	No	Low	Negative	Benign
08/07/98	Physician	Yes	No	High	Positive	Benign
02/07/97	Herself	No	No	Low	Negative	Normal
03/05/97	Herself	Yes	Yes	Low	Negative	Benign (fibroadenoma)
07/26/97	Herself	No	No	Low	Negative	Normal
11/16/97	Herself	Yes	Yes	Low	Negative	Benign (fibroadenoma)
12/14/97	Herself	No	No	Low	Negative	Normal

Normal: normal subject who does not have any tumor based on reliable health history; Abnormal mass type: determined based on biopsy or reliable health history.

pulses. However, they also pointed out that adiabatic pulses must have long pulse widths to produce good slice profiles. Long pulse widths can lead to a greater magnetization transfer effect (27), which in the current study was assumed to be relatively small. In addition, it is not practical to use long RF pulses as the acquisition pulses in 2D fast SPGR, because of the resulting long total image acquisition times. Flowing spins during RF application can also affect the slice profiles generated by long RF pulses. Therefore, SLR pulses were used in this study because they can provide sharp slice profiles with relatively shorter pulse widths. The perfusion quantification error due to slice profile imperfection is reduced through the semi-log linear regression data processing. This technique is different from that presented by Sidaros et al. (29), which requires the precise knowledge of the inversion pulses for the offset estimation. The current regression technique does not require prior knowledge of the RF pulse profiles. It only assumes that the signal contamination at the selective sequence is caused by signal from noninverted spins. The regression is straightforward and provides the statistical information to justify the confidence level of the f/λ estimation for each pixel.

The fast SPGR-based spin tagging sequence, and the new data analysis technique have some limitations for estimating T_1 and f/λ accurately. It was assumed that the data acquisition would not disturb the recovery curves of the inverted spins or the equilibrium states of the noninverted spins. To make this assumption more realistic, we investigated replacing the 2D fast SPGR data acquisition scheme with an echo-planar or spiral data acquisition scheme. In echo-planar imaging (EPI) or spiral imaging, only one acquisition RF pulse is used for the complete data acquisition of a whole image. The disturbance resulting from the acquisition RF pulses to the recovery curves of the inverted spins or the equilibrium of the noninverted spins is therefore smaller. Since EPI or spiral imaging is faster than 2D fast SPGR, the total scan time is shorter also. However, both EPI and spiral imaging are sensitive to system imperfections, such as eddy currents. The fast SPGR is less sensitive to system imperfections, and thus was chosen as the data acquisition scheme in this work. The T_1 of blood is assumed to be the same as that of tissue. Since the T_1 of blood is longer than the T_1 of tissue, this assumption leads to some overestimation of the f/λ by a factor difference (23). This factor difference does not affect the graphs and statistical analyses that were done to separate probable malignant from benign tissue.

In MRI, the technique that is most widely used for breast cancer detection is MR dynamic first-pass contrast enhancement (commonly called MR mammography). This technique has shown its ability to distinguish between malignant and benign breast lesions (30). However, it cannot be used in screening, even within defined high-risk subpopulations (e.g., patients with dense breasts), due to the high cost of administering contrast material. Furthermore, the scan must be completed within a limited time to avoid the washout of contrast material, which limits the resolution and SNR. The AST technique presented here does not require contrast materials, and potentially can be used as a screening tool. It may provide more sensitive and specific assessments of tissue parameters, at higher spatial resolutions, by its ability to improve SNR over a reasonable scan time. The current AST pulse sequence and analytical techniques may be suitable for all specific clinical indications that have been described for first-pass contrast-enhanced imaging. They may, in fact, be more convenient and equally reliable for identifying the regions of tissue changes that give rise to contrast enhancement. However, contrast enhancement is regarded as essential in MRI breast evaluation, and is unlikely to be supplanted. We recommend that first-pass contrast enhancement compar-

ison studies be performed along with the AST methods. This would allow the direct comparison in accuracy, precision as well as the ease of application.

ACKNOWLEDGMENTS

The authors thank Dr. Rebecca A. Zulim for referring patients to the breast studies.

APPENDIX

Derivation of the Semi-log Linear Regression Equations

In the derivation of the linear equations (Eqs. [7] and [8]), the following ideal situation is assumed: The acquisition RF pulse causes such a small flip angle that its continuous application for all the phase-encoding steps does not disturb the natural recovery of the inverted spins of a tagging sequence and the equilibrium of the spins at the nontagging sequence.

Given this assumption, for a spin tagging sequence, the steady-state longitudinal magnetization at the end of each TR period just before the next inversion pulse can be stated as:

$$M_{t0ss} = M_0 \frac{1 - e^{-R_1 \mathrm{TR}}}{1 + e^{-R_1 \mathrm{TR}}} \qquad [A1]$$

where M_{t0ss} = the steady-state longitudinal magnetization at the end of each TR period, and M_0 = the longitudinal magnetization under fully relaxed conditions,

$$R_1 = \begin{cases} \dfrac{1}{T_{1s}} & \text{for the selective condition} \\ \dfrac{1}{T_{1n}} & \text{for the nonselective condition} \end{cases},$$

TR = the repetition time.

The longitudinal magnetization at time t after the spin inversion at steady state is

$$M_t(t) = M_0(1 - e^{-R_1 t}) - M_{t0ss} e^{-R_1 t} = M_0\left(1 - \frac{2e^{-R_1 t}}{1 + e^{-R_1 \mathrm{TR}}}\right)$$

or

$$M_t(t) = M_0\left(1 - \frac{2e^{-R_1 t}}{1 + e^{-R_1 \mathrm{TR}}}\right). \qquad [A2]$$

As a result, the signal measured at TE is

$$S_t = M_0\left(1 - \frac{2e^{-R_1 \mathrm{TI}}}{1 + e^{-R_1 \mathrm{TR}}}\right)\sin(\theta)e^{-(\mathrm{TE}/T2)} \qquad [A3]$$

where TI is the time of inversion, TE is the time of echo at each acquisition period, and θ is the acquisition RF flip angle.

For the spin nontagging sequence, based on the given assumption, the longitudinal magnetization $M_{nt}(t)$ at any time t stays at equilibrium. Specifically,

$$M_{nt}(t) = M_0. \qquad [A4]$$

The signal measured at TE becomes

$$S_{nt} = M_0 \sin(\theta) e^{-(\mathrm{TE}/T2)} \qquad [A5]$$

Thus,

$$\frac{S_t}{S_{nt}} = 1 - \frac{2e^{-R_1 \mathrm{TI}}}{1 + e^{-R_1 \mathrm{TR}}}. \qquad [A6]$$

Then,

$$\frac{S_{nt} - S_t}{S_{nt}} = \frac{2e^{-R_1 \mathrm{TI}}}{1 + e^{-R_1 \mathrm{TR}}}.$$

Thus,

$$\frac{S_{nt} - S_t(i)}{S_{nt} - S_t(j)} = \frac{e^{-R_1 \mathrm{TI}(i)}}{e^{-R_1 \mathrm{TI}(j)}} = e^{-R_1(\mathrm{TI}(i) - \mathrm{TI}(j))} \qquad [A7]$$

where TI(i) = the time of inversion at the ith TI cycle, $S_t(i)$ = the signal at a pixel when TI(i) is used, TI(j) = the time of inversion at the jth TI cycle, and $S_t(j)$ = the signal at a pixel when TI(j) is used.

Then,

$$\ln(S_{nt} - S_t(i)) - \ln(S_{nt} - S_t(j)) = -R_1(\mathrm{TI}(i) - \mathrm{TI}(j)).$$

Thus,

$$R_1 = -\frac{\ln(S_{nt} - S_t(i)) - \ln(S_{nt} - S_t(j))}{\mathrm{TI}(i) - \mathrm{TI}(j)}. \qquad [A8]$$

The above equation shows the semi-log linear regression relationship between ($S_{nt} - S_t$) and TI. It can be applied to both selective and nonselective tagging sequences.

RF Slice Profile Mismatch Analysis

From Eq. [9],

$$\frac{S_{sel_{meas}}}{S_{nt}} = (1 - err)\frac{S_{sel}}{S_{nt}} + err$$

and

$$\frac{S_{sel}}{S_{nt}} = \frac{\dfrac{S_{sel_{meas}}}{S_{nt}} - err}{1 - err}$$

$$1 - \frac{S_{sel}}{S_{nt}} = 1 - \frac{\dfrac{S_{sel_{meas}}}{S_{nt}} - err}{1 - err}$$

$$\frac{S_{nt} - S_{sel}}{S_{nt}} = \frac{1 - err - \dfrac{S_{sel_{meas}}}{S_{nt}} + err}{1 - err}$$

$$= \frac{1 - \dfrac{S_{sel_{meas}}}{S_{nt}}}{1 - err}.$$

Thus,

$$\frac{S_{nt} - S_{sel}(i)}{S_{nt} - S_{sel}(j)} = \frac{1 - \dfrac{S_{sel_{meas}}(i)}{S_{nt}}}{1 - \dfrac{S_{sel_{meas}}(j)}{S_{nt}}}$$

$$= \frac{S_{nt} - S_{sel_{meas}}(i)}{S_{nt} - S_{sel_{meas}}(j)}. \quad [A9]$$

Therefore,

$$\ln(S_{nt} - S_{sel}(i)) - \ln(S_{nt} - S_{sel}(j)) = \ln(S_{nt} - S_{sel_{meas}}(i)) - \ln(S_{nt} - S_{sel_{meas}}(j)). \quad [A10]$$

REFERENCES

1. Buonocore MH, Zhu DC, Barakat-Pellot C. Measurement of breast tissue perfusion using arterial spin tagging. In: Proceedings of the 5th Annual Meeting of ISMRM, Vancouver, Canada, 1997. p 311.
2. Zhu DC, Buonocore MH, Barakat-Pellot C. Breast tissue differentiation using arterial spin tagging. In: Proceedings of the 1997 UC Davis Biomedical Engineering Symposium, Davis, 1997. p 35–36.
3. Buonocore MH, Zhu DC, Pellot-Barakat C, Zulim RA. Non-invasive measurement of breast tissue perfusion using arterial spin tagging. Radiology 1997;205:162.
4. Buonocore MH, Zhu DC, Zulim RA. Analysis software for breast imaging studies. In: Proceedings of the 7th Annual Meeting of ISMRM, Philadelphia, 1999. p 2172.
5. Zhu DC. Magnetic resonance pulse sequences and analytical techniques for breast cancer detection and cardiovascular flow. Doctoral dissertation, University of California–Davis, Davis, California, 1999.
6. Buonocore MH, Zhu DC. Magnetic resonance arterial spin tagging for non-invasive pharmacokinetic analysis of breast cancer. In: Proceedings of the Era of Hope, Dept. of Defense Breast Cancer Research Program Meeting, Atlanta, GA, 2000. p 177.
7. Folkman J, Merler E, Abernathy C, Williams G. Isolation of a tumor factor responsible for angiogenesis. J Exp Med 1971;133:275–288.
8. Kallinowski F, Schlenger KH, Runkel S, Kloes M, Stohrer M, Okunieff P, Vaupel P. Blood flow, metabolism, cellular microenvironment and growth rate of human tumor xenografts. Cancer Res 1989;49:3759–3764.
9. Gimbrone Jr MA, Leapman SB, Cotran RS, Folkman J. Tumor dormancy *in vivo* by prevention of neovascularization. J Exp Med 1972;136:261–276.
10. Jain RK. Determinants of tumor blood flow: a review. Cancer Res 1988;48:2641–2658.
11. Edelman RR, Zlatkin MB, Hesselink JR. Clinical magnetic resonance imaging, 2nd ed. Philadelphia: W.B. Saunders Company; 1996.
12. Kety SS, Schmidt CF. The determination of cerebral blood flow in man by the use of nitrous oxide in low concentrations. Am J Physiol 1945; 143:53–66.
13. Kety SS. Measurement of local blood flow by the exchange of an inert diffusible substance. Methods Med Res 1960;8:226–236.
14. Kety SS. The theory and applications of the exchange of inert gas at the lungs and tissues. Pharmacol Rev 1951;3:1–41.
15. Detre JA, Leigh LS, Williams DS, Koretsky AP. Perfusion imaging. Magn Reson Med 1992;23:37–45.
16. Detre JA, Zhang W, Roberts DA, Silva AC, Williams DS, Grandis DJ, Koretsky AP, Leigh JS. Tissue specific perfusion imaging using arterial spin labeling. NMR Biomed 1994;7:75–82.
17. Kim S. Quantification of relative cerebral blood flow change by flow-sensitive alternating inversion recovery (FAIR) technique: application to functional mapping. Magn Reson Med 1995;34:293–301.
18. Kwong KK, Chesler DA, Weisskoff RM, Donahue KM, Davis TL, Ostergaard L, Campbell TA, Rosen BR. MR perfusion studies with T_1-weighted echo planar imaging. Magn Reson Med 1995;34:878–887.
19. Wong EC, Buxton RB, Frank LR. Quantitative imaging of perfusion using a single subtraction (QUIPSS and QUIPSS II). Magn Reson Med 1998;39:702–708.
20. Barbier EL, Silva AC, Kim HJ, Williams DS, Koretsky AP. Perfusion analysis using dynamic arterial spin labeling. Magn Reson Med 1999; 41:299–308.
21. Bauer WR, Hiller KH, Roder F, Rommel E, Ertl G, Haase A. Magnetization exchange in capillaries by microcirculation affects diffusion-controlled spin-relaxation: a model which describes the effect of perfusion on relaxation enhancement by intravascular contrast agents. Magn Reson Med 1996;35:43–55.
22. Bauer WR, Roder F, Hiller KH, Han H, Frohlich S, Rommel E, Haase A, Ertl G. The effect of perfusion on T_1 after slice-selective spin inversion in the isolated cardioplegic rat heart: measurement of a lower bound of intracapillary-extravascular water proton exchange rate. Magn Reson Med 1997;38:917–923.
23. Belle V, Kahler E, Waller C, Rommel E, Voll S, Hiller KH, Bauer WR, Haase A. In vivo quantitative mapping of cardiac perfusion in rats using a noninvasive MR spin-labeling method. J Magn Reson Imaging 1998;8:1240–1245.
24. Pauly J, Le Roux P, Nishimura D, Macovski A. Parameter relations for the Shinnar-Le Roux selective excitation pulse design algorithm. IEEE Trans Med Imaging 1991;10:53–65.
25. Duda RO, Hart PE, Stork DG. Pattern classification and scene analysis, 2nd ed. University of California–Davis, Davis, CA: Department of Electrical and Computer Engineering; 1997.
26. Buxton RB, Frank LR, Wong EC, Siewert B, Warach S, Edelman RB. A general kinetic model for quantitative perfusion imaging with arterial spin labeling. Magn Reson Med 1998;40:383–396.
27. Frank LR, Wong EC, Buxton RB. Slice profile effects in adiabatic inversion: application to multislice perfusion imaging. Magn Reson Med 1997;38:558–564.
28. Schepers J, Garwood M, van der Sanden B, Nicolay K. Improved subtraction by adiabatic FAIR perfusion imaging. Magn Reson Med 2002; 47:330–336.
29. Sidaros K, Andersen IK, Gesmar H, Rostrup E, Larsson HBW. Improved perfusion quantification in FAIR imaging by offset correction. Magn Reson Med 2001;46:193–197.
30. Kaiser WA. MR mammography. Berlin: Springer-Verlag; 1993.